

# Orbital mixing and nesting in the bilayer manganites $\text{La}_{2-2x}\text{Sr}_{1+2x}\text{Mn}_2\text{O}_7$

R. Saniz,<sup>1,\*</sup> M. R. Norman,<sup>2</sup> and A. J. Freeman<sup>1</sup>

<sup>1</sup>*Department of Physics and Astronomy, Northwestern University, Evanston, Illinois 60208*

<sup>2</sup>*Materials Science Division, Argonne National Laboratory, Argonne, Illinois 60439*

(Dated: May 29, 2019)

A first principles study of  $\text{La}_{2-2x}\text{Sr}_{1+2x}\text{Mn}_2\text{O}_7$  compounds for doping levels  $0.3 \leq x \leq 0.5$  shows that the low energy electronic structure of the majority spin carriers is determined by strong momentum dependent interactions between the Mn  $e_g$   $d_{x^2-y^2}$  and  $d_{3z^2-r^2}$  orbitals, that differ in the ferromagnetic and antiferromagnetic phases. The resulting Fermi surface exhibits nesting behavior that is reflected by peaks in the static susceptibility, whose positions as a function of momentum have a non-trivial dependence on the doping level  $x$ .

PACS numbers: 71.18.+y, 71.20.-b, 75.40.Gb, 75.47.Lx

One of the most studied series of compounds over the past decade is that of the bilayer manganites  $\text{La}_{2-2x}\text{Sr}_{1+2x}\text{Mn}_2\text{O}_7$ , which have been scrutinized using a wide range of experimental methods [1], with new findings of their basic properties continuing to emerge [2, 3]. The interest in these systems arises for several reasons. It is well known that they exhibit a colossal magnetoresistive effect around critical temperatures of 100-200 K, depending on the doping level  $x$  [1]. A proper understanding of this phenomenon should point the way to tailoring materials with higher critical temperatures, which could potentially lead to magnetic devices that would outperform present ones based on the giant magnetoresistive effect. On the fundamental side, it is thought that the properties of these materials are due to an interplay of structural, orbital, and magnetic degrees of freedom, a trait shared by several strongly correlated materials, including the superconducting cuprates [4]. In the case of the manganites, there is no consensus as yet on exactly how these different degrees of freedom lead to the observed properties. Elucidating this will no doubt lead to an advance in our understanding of related phenomena in the broader context of condensed matter systems of higher complexity.

One of the reasons for the current state of affairs is that the ground state properties of the bilayer manganites are not completely understood, even at low temperatures. From the theoretical point of view, there are few published reports of *ab initio* calculations of the electronic structure of these compounds [5]. While these studies have provided an important framework for the analysis of experiments, several observations remain to be addressed. For instance, it is generally recognized that it is the character of the occupied Mn  $e_g$  states that determines the key properties of these systems, such as the conductivity and the nature of the magnetic order. Thus, important efforts have been made to understand the orbital polarization of these states [6, 7, 8, 9], but the problem has only been partially addressed from an *ab initio* perspective [10]. In this work, we present a first principles study of the conducting states of the bilayer

manganites for doping levels  $0.3 \leq x \leq 0.5$ . We show that the  $d_{x^2-y^2}$  and  $d_{3z^2-r^2}$  orbitals strongly mix, with the mixing depending not only on the hole doping level, but also on the direction in  $\mathbf{k}$ -space. This has a pronounced impact on the Fermi surface topology and nesting, long suggested to play an important role in the properties of these materials [11, 12, 13]. This is illustrated by calculating the static susceptibility as a function of momentum, which indeed shows peaks due to nesting. The implications of our work in relation to recent experiments are discussed.

We employ the highly precise all-electron full-potential linearized augmented plane wave (FLAPW) implementation of density functional theory [14], with the generalized gradient approximation [15] for the exchange-correlation potential. For  $x < 0.5$ , we use the “charged cell” approximation, i.e., increasing the valence electron number by the required amount and adding a uniform positive charge for neutrality [16]. The calculations were carried out for the observed magnetic phases: ferromagnetic (FM) for  $x \leq 0.4$  and antiferromagnetic (AF) for  $x \geq 0.45$ . In our calculations, the AF phase is given by ferromagnetic  $\text{MnO}_2$  planes that are coupled antiferromagnetically within a bilayer as well as between adjacent bilayers. Although in experiment the latter coupling is ferromagnetic in the A-type AF order, it is known to be very weak [1], and so should not influence our results. As for technical aspects of the calculations, convergence was assured with respect to muffin-tin radii,  $\mathbf{k}$ -point mesh [1164 points in the irreducible wedge of the Brillouin zone], and energy cut-offs. The structural parameters ( $I4/mmm$  space group) are those of Ref. 17 at 10 K. We assume that La is in the  $2b$  site and Sr in the  $4e$  sites [18].

As indicated above, a key feature in the understanding of the bilayer manganites is the relative role of the  $e_g$  states ( $d_{x^2-y^2}$  and  $d_{3z^2-r^2}$ ) [1]. To illustrate these states, we refer to the band structure plots in Fig. 1 (simple tetragonal symmetry notation is used). Two cases are shown, namely  $x = 0.5$  (AF) and  $x = 0.4$  (FM). The states with more than 50% Mn d character are highlighted with dots. In the AF case, there is Kramers de-

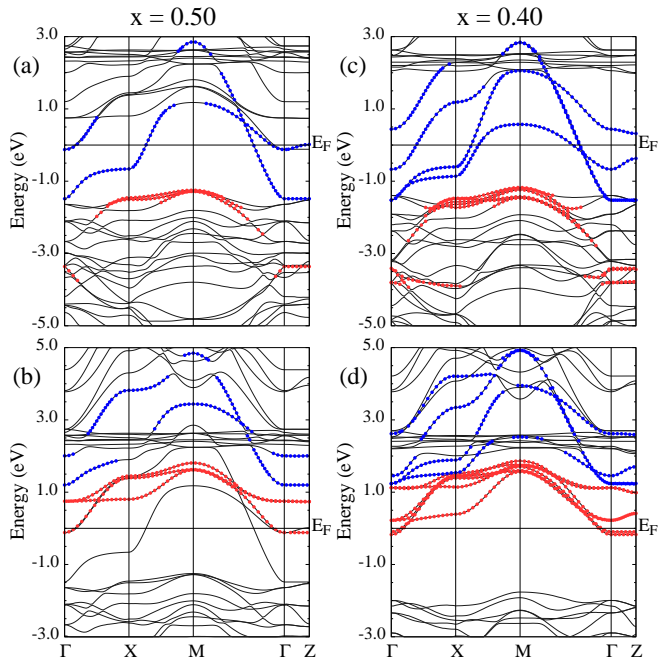


FIG. 1: (color online) Band structure of  $\text{LaSr}_2\text{Mn}_2\text{O}_7$  ( $x = 0.5$ , AF phase) for  $\uparrow$  [ $\downarrow$ ] spin in panel (a) [(b)], and of  $\text{La}_{1.2}\text{Sr}_{1.8}\text{Mn}_2\text{O}_7$  ( $x = 0.4$ , FM phase) for  $\uparrow$  [ $\downarrow$ ] spin in panel (c) [(d)]. The gray (red) and black (blue) dots highlight states of dominant Mn  $t_{2g}$  and  $e_g$  character, respectively.

generacy, so the two spin states are interchanged for the second Mn atom type (there is only one Mn atom type in the FM case). In the following, we focus on the  $e_g$  states.

The basic electronic structure of the majority spin states near the Fermi energy ( $E_F$ ) can be understood as arising from the two Mn  $d_{x^2-y^2}$  and two Mn  $d_{3z^2-r^2}$  orbitals per bilayer. If we ignore orbital mixing and hybridization with other states, then in the FM case, the energy of each orbital would be of the form  $\epsilon_i \pm X \pm \Delta$  where  $\epsilon_i$  is the unpolarized atomic orbital energy ( $i = 1, 2$ ),  $2X$  the exchange splitting, and  $2\Delta$  the bilayer splitting, resulting in eight states altogether. In contrast, for the AF case, the energy of each orbital would be of the form  $\epsilon_i \pm \sqrt{X^2 + \Delta^2}$  resulting in four Kramers degenerate states. Since  $X \gg \Delta$ , the bilayer splitting is essentially quenched in the AF case. As a consequence, as we show below, there is only one barrel centered at M in the AF case, as opposed to two in the FM case. Moreover, for the AF case, unlike the FM one, we do not expect a strong intensity modulation of the photoemission signal as a function of photon energy due to bilayer splitting.

In the actual calculations, though, the two  $e_g$  orbitals are mixed. This is directly reflected in the Fermi surface topology. In Fig. 2(a), we show the Fermi surface for  $x = 0.5$  (AF), and in Fig. 2(b) for  $x = 0.4$  (FM, majority spin). In the AF case, there is a hole-like barrel centered at M of mainly  $d_{x^2-y^2}$  symmetry (labeled 1), a prolate electron-like sheet around  $\Gamma$  of  $d_{3z^2-r^2}$  symmetry (labeled

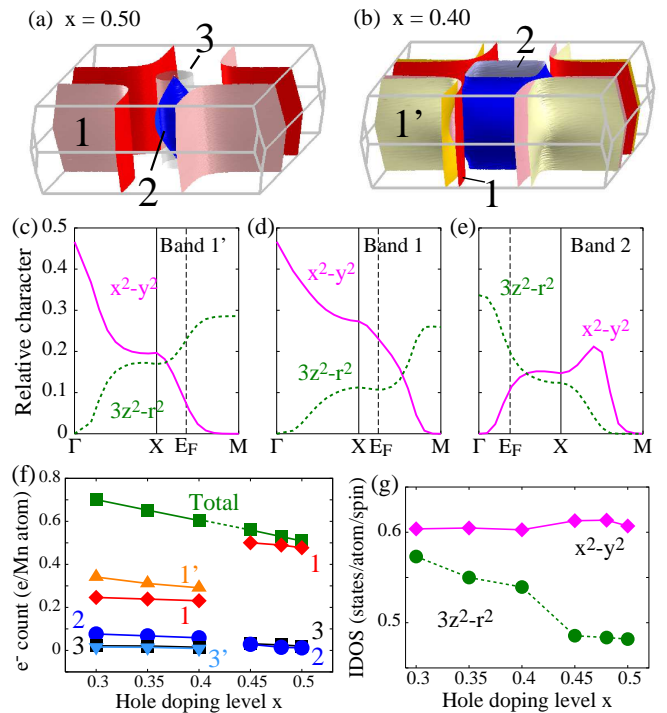


FIG. 2: (color online) Fermi surface for (a)  $x = 0.5$  (AF) and (b)  $x = 0.4$  (FM). The surface labels are explained in the text. (c), (d), and (e): Orbital character of the states along the  $\Gamma$ -X-M line for the  $e_g$  bands crossing  $E_F$  for  $x = 0.4$ . (f) Luttinger count of the different Fermi surface sheets, and (g) total occupations (integrated density of states, IDOS) for  $d_{x^2-y^2}$  and  $d_{3z^2-r^2}$  as a function of doping.

2), and a (minority spin) cylindrical sheet centered at  $\Gamma$  of  $d_{xy}$  symmetry (labeled 3). In the FM phase, there is a hole-like barrel of dominant  $d_{x^2-y^2}$  symmetry centered at M (labeled 1), and two sheets of strongly hybridized  $d_{x^2-y^2}$  and  $d_{3z^2-r^2}$  symmetry: a hole-like barrel centered at M (labeled 1') and an electron-like barrel centered at  $\Gamma$  (labeled 2) [19].

The mixing is shown by an analysis of the character of the states corresponding to the bands crossing  $E_F$ . For example, in Fig. 2(c) we show the character of the lower  $e_g$  band (1') for  $x = 0.4$  (FM) and  $\mathbf{k}$  points along the  $\Gamma$ -X-M directions. It starts with  $d_{x^2-y^2}$  character at  $\Gamma$ , but when reaching X, the mixing with  $d_{3z^2-r^2}$  is about 50%. At  $E_F$ , about halfway from X toward M, the character becomes dominantly  $d_{3z^2-r^2}$ . The middle band (1), in contrast [Fig. 2(d)], has a fairly dominant  $d_{x^2-y^2}$  character up to  $E_F$ , at about a quarter of the X-M distance. Band 2, in turn [Fig. 2(e)], starts out at  $\Gamma$  as  $d_{3z^2-r^2}$  but is strongly mixed at  $E_F$ . Thus, it is inaccurate to characterize the barrels around the M point as ' $x^2 - y^2$ ', and the electron pocket around  $\Gamma$  as ' $3z^2 - r^2$ '. Our results for the other doping levels in the FM phase indicate that the orbital mixing tends to increase with decreasing hole doping, and that the bilayer

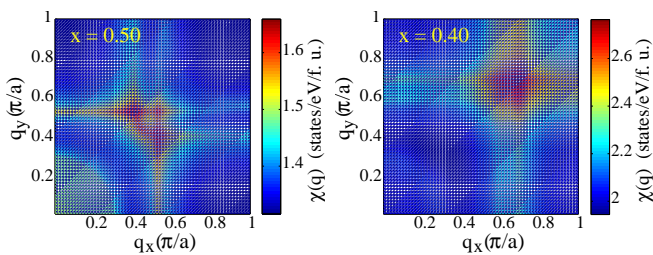


FIG. 3: (color online) The static susceptibility,  $\chi(\mathbf{q})$ , for  $\mathbf{q} = (q_x, q_y, 2\pi/c)$ , for  $x = 0.5$  (AF) and  $x = 0.4$  (FM).

splitting becomes stronger. A similar analysis shows that in the AF case, the lower  $e_g$  band (1) is dominantly of  $d_{x^2-y^2}$  character, but with strong mixing at  $E_F$  along X-M. The upper band (2) is  $d_{3z^2-r^2}$  like.

Of further relevance to experiment is the occupation level of the several bands crossing  $E_F$ . Thus, we calculated the carrier number by integrating the volume enclosed by the different Fermi surfaces (the Luttinger count). We used a fine mesh of 32340  $\mathbf{k}$ -points in the irreducible wedge, and the results as a function of doping are shown in Fig. 2(f) (lines are a guide to the eye only). In the AF phase, sheet 1 is obviously dominant. When switching to the FM phase, the Kramers degeneracy is lifted, giving rise to sheets 1 and 1'. The increased orbital mixing lowers the energy, particularly in the case of states 1', allowing the charge to increase as  $x$  decreases. In the FM phase there is only one sheet 2 because the antibonding counterpart is empty (due to the large bilayer splitting of  $3z^2 - r^2$  in the FM phase). Thus, the electron pocket around  $\Gamma$  roughly doubles in size compared to the AF phase. Note that for  $0.4 < x \lesssim 0.45$  the actual phase is a canted antiferromagnet [17], so the bilayer splitting is probably gradually quenched with doping. But clearly, AF coupling nullifies the bilayer splitting, with dramatic effects, particularly for the  $d_{3z^2-r^2}$  states. This is in line with very recent photoemission data regarding the collapse of bilayer splitting close to  $x = 0.4$  [20].

To summarize, the  $d_{x^2-y^2}$  orbital population is not strongly affected across the FM-AF transition, but the  $d_{3z^2-r^2}$  orbital population significantly increases in the FM phase. This is shown in Fig. 2(g), where we plot the occupation counts (estimated by integrating the muffin-tin projected density of states) of the two orbitals as a function of  $x$ . These results coincide with conclusions from magnetic Compton scattering measurements [6]. We stress that the invariance of the  $d_{x^2-y^2}$  count with  $x$  is a definite departure from rigid band behavior.

The above results also indicate that the possible nesting instabilities suggested to play an important role in these materials [11, 13] have a non-trivial dependence on  $x$ . To see this, we calculated the generalized charge

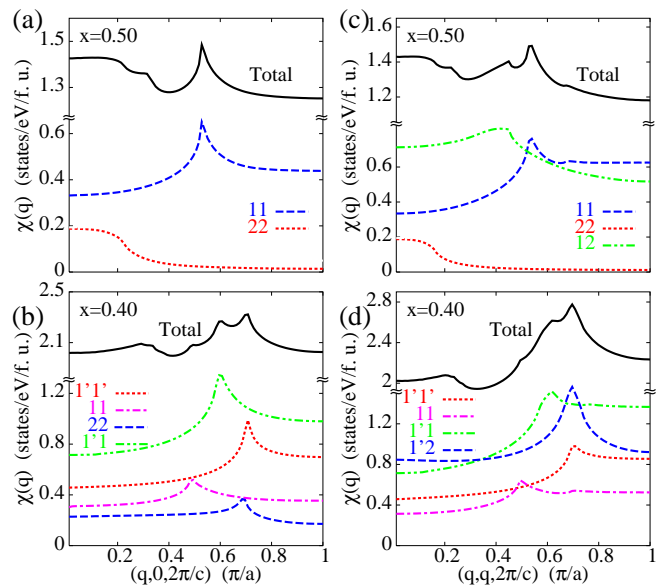


FIG. 4: (color online) Static susceptibility  $\chi(\mathbf{q})$  for  $\mathbf{q}$  along two symmetry directions for  $x = 0.5$  (AF) and  $x = 0.4$  (FM). The labels indicate which band transitions are responsible for the structure in  $\chi$ . Labeling corresponds to that in Fig. 2. Note the break in the vertical axis.

susceptibility (constant matrix element approximation)

$$\chi(\mathbf{q}, \omega \rightarrow 0) = \frac{1}{N} \sum_{n,m} \sum_{\mathbf{k}, \sigma} \frac{f_{n\mathbf{k}\sigma}(1 - f_{m\mathbf{k}+\mathbf{q}\sigma})}{\epsilon_{m\mathbf{k}+\mathbf{q}\sigma} - \epsilon_{n\mathbf{k}\sigma} - \omega}. \quad (1)$$

For this calculation, we again used 32340  $\mathbf{k}$ -points in the irreducible wedge and the tetrahedron method with linear interpolation [21]. In Fig. 3, we show  $\chi(\mathbf{q})$  for  $\mathbf{q}$  of the form  $(q_x, q_y, 2\pi/c)$ . This is of interest because diffuse x-ray scattering data have shown peaks for  $q_z = 2\pi/c$  in the  $x = 0.4$  compound [22]. Both the AF and FM cases show clear peaks and kinks correlating closely with the topology of the Fermi surface. The calculations were done taking into account only the bands crossing  $E_F$ . We verified that including more bands does not affect significantly the momentum structure of the response. Also, the  $e_g$  to  $t_{2g}$  transitions were ignored to crudely simulate the neglected matrix elements. We note that the  $t_{2g}$  transitions mostly contribute to a diffuse response centered at  $\Gamma$ , so we focus on the  $e_g$  transitions only.

Figure 4 takes a closer look for  $\mathbf{q}$  along two directions. For  $\mathbf{q} = (q, 0, 2\pi/c)$ , Fig. 4(a) (AF) shows a strong peak at  $q = 0.53$  (11 transition). The interband transition (12) has little structure (not shown). Figure 4(b) (FM) shows two main peaks, for  $q = 0.62$  (1'1' transition), and  $0.71$  (1'1' and 22 transitions). The peak arising from 11 transitions is relatively weaker in the FM case. It is significant that the 1'1' peak at this doping level matches the bond centered peak reported at  $q = 0.6$  in Ref. 22. For  $\mathbf{q} = (q, q, 2\pi/c)$ , Fig. 4(c) (AF) shows the same (11) peak as Fig. 4(a), and a less well defined maximum at

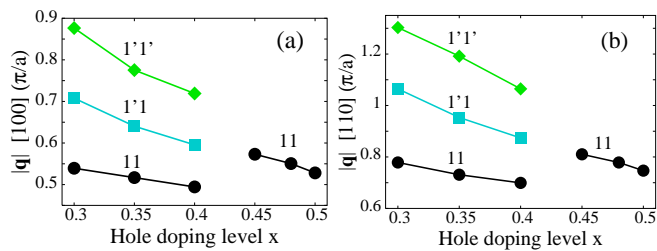


FIG. 5: (color online) Nesting vector lengths (extracted from the peaks in  $\chi$ ) as a function of doping level  $x$  for  $\mathbf{q}$  along (a) the [100] and (b) [110] directions.

$q = 0.42$  (12 transition). This maximum is equally ill-defined at other doping levels. Fig. 4(d) (FM) shows a clearly dominant peak at  $q = 0.7$  arising from mainly 1'1' and 1'2 transitions. We point out that the two kinks for smaller  $q$  (1'1 and 11) are weaker at lower doping levels because of strong broadening of these features.

Finally, in Fig. 5 we consider the doping dependence of the lengths of the nesting vectors for  $\mathbf{q}$  along the [100] and [110] directions, which were inferred from photoemission [11, 12]. The nesting vectors are extracted from the peaks in  $\chi$  corresponding to those in Fig. 4. Again, we remark that we do not have results for the actual canted phase for  $0.45 \lesssim x < 0.5$ . Note that the 11 vector for  $x = 0.4$  in the [110] direction matches that of the so-called CE-ordering wave vector [11]. We particularly point to the jump of the 11 nesting vector when going from the FM to the AF phase. Clearly, this is due to the ‘turning on’ of the bilayer splitting in the FM phase. Again, this illustrates dramatically the correlation between  $d_{3z^2-r^2}$  and  $d_{x^2-y^2}$  orbital mixing, bilayer splitting, and FM order. Further, the discontinuity just mentioned may help explain the non-monotonic dependence of the nesting vector with  $x$  recently inferred from photoemission [23] and diffuse scattering measurements [24]. The charge ordering peaks observed in diffuse scattering [24] are either along the bond direction, the diagonal, or both, depending on the doping level. Typically, we find that the diagonal response is largest, since although the nesting is not as good for such vectors, twice as many faces of the Fermi surface are brought into coincidence as compared to the bond oriented case [25]. We also point out that in the FM phase, for transitions involving 1', the peak structure for  $q_z = 0$  along the bond direction is less distinct than for  $q_z = 2\pi/c$ . This is because of the ‘tilting’ of the 1' surface (a consequence of the strong  $d_{3z^2-r^2}$  admixture for this surface) which alternates in direction between  $k_z = 0$  and  $k_z = 2\pi/c$  due to the  $c$ -axis dispersion. For the same reason, the diagonal peaks involving 1' are stronger for  $q_z = 0$ . This may explain why the diffuse scattering peaks occur for  $q_z = 2\pi/c$  for the bond directions and  $q_z = 0$  for the diagonal directions [22, 24].

In summary, we find that mixing of the Mn  $d_{x^2-y^2}$  and

$d_{3z^2-r^2}$  orbitals and bilayer splitting play a fundamental role in the electronic structure of the bilayer manganites, particularly in the FM phase, and correlate closely with the transition from FM to AF order with doping. These two effects result in different Fermi surface topologies for the two phases. As a result, the static susceptibility, and the  $e_g$  orbital polarization, are predicted to have a non-monotonic dependence on doping due to the change from ferromagnetism to antiferromagnetism as the hole doping level increases.

We acknowledge the support of the US DOE, Office of Science, under Grant No. DE-FG02-88ER45372 and Contract No. DE-AC02-06CH11357, and a computer time grant at the National Energy Research Scientific Computing Center. We thank B. Barbiellini, L.-H. Ye, J.-H. Song, J. F. Mitchell, R. Osborn, S. Rosenkranz, U. Chatterjee and J. C. Campuzano for useful discussions.

---

\* Present address: Departement Fysica, Universiteit Antwerpen, Groenenborgerlaan 171, B-2020 Antwerpen, Belgium.

- [1] T. Kimura and Y. Tokura, *Annu. Rev. Mater. Sci.* **30**, 451 (2000).
- [2] N. Mannella *et al.*, *Phys. Rev. B* **76**, 233102 (2007).
- [3] S. de Jong *et al.*, *Phys. Rev. B* **76**, 235117 (2007).
- [4] E. Dagotto, *Science* **309**, 257 (2005).
- [5] X. Y. Huang *et al.*, *Phys. Rev. B* **62**, 13318 (2000).
- [6] A. Koizumi *et al.*, *Phys. Rev. Lett.* **86**, 5589 (2001).
- [7] Y. Li *et al.*, *Phys. Rev. Lett.* **93**, 207206 (2004).
- [8] B. Barbiellini *et al.*, *J. Phys. Chem. Solids* **66**, 2197 (2005).
- [9] A. Koizumi *et al.*, *Phys. Rev. B* **74**, 012408 (2006).
- [10] P. E. Mijnaerends *et al.*, *Phys. Rev. B* **75**, 014428 (2007).
- [11] Y.-D. Chuang *et al.*, *Science* **292**, 1509 (2001).
- [12] Z. Sun *et al.*, *Phys. Rev. Lett.* **97**, 056401 (2006).
- [13] M. W. Kim *et al.*, *Phys. Rev. Lett.* **98**, 187201 (2007).
- [14] E. Wimmer *et al.*, *Phys. Rev. B* **24**, 864 (1981); H. J. F. Jansen and A. J. Freeman, *ibid.* **30**, 561 (1984).
- [15] J. P. Perdew, K. Burke, and M. Ernzerhof, *Phys. Rev. Lett.* **77**, 3865 (1996).
- [16] A calculation following the same scheme was used with great success to explain the trends with doping level in  $\text{La}_x\text{Ca}_{1-x}\text{MnO}_3$ . See W. Luo *et al.*, *Phys. Rev. Lett.* **99**, 036402 (2007).
- [17] M. Kubota *et al.*, *J. Phys. Soc. Jpn.* **69**, 1606 (2000).
- [18] R. Seshadri *et al.*, *Solid State Commun.* **101**, 453 (1997).
- [19] In the FM case, the states of  $d_{xy}$  symmetry (minority spin) result in two slightly split cylinders (3 and 3') around  $\Gamma$  [not shown in Fig. 2(b)].
- [20] C. Jozwiak *et al.*, preprint arXiv:0806.2120.
- [21] J. Rath and A. J. Freeman, *Phys. Rev. B* **11**, 2109 (1975).
- [22] L. Vasiliu-Doloc *et al.*, *Phys. Rev. Lett.* **83**, 4393 (1999); B. J. Campbell *et al.*, *Phys. Rev. B* **65**, 014427 (2001).
- [23] D. S. Dessau, private communication.
- [24] S. Rosenkranz, private communication.
- [25] H. J. Schulz, *Phys. Rev. Lett.* **64**, 1445 (1990).